Computing creep-damage interactions in irradiated concrete

Alain B. Giorla*[a] and Yann Le Pape[a] and Cyrille F. Dunant[b]

[a] Oak Ridge National Laboratory, One Bethel Valley Road, Oak Ridge, TN 37831, USA
[b] Ecole Polytechnique Fédérale de Lausanne, Lausanne, Switzerland
* corresponding author. Email address: giorlaab@ornl.gov

Abstract

Among the various degradation mechanisms possibly affecting the long-term operation of nuclear power plants, the effects of induced expansion and internal degradation that occur in concrete exposed to high-flux neutron radiation require additional research. Notably, the utilization of short-term test-reactor data to assess the long-term structural significance of light water reactor concrete biological shields necessitates to properly capture the concurrent time-dependent effects, e.g., creep and damage caused by radiation-induced volumetric damage. As this poses significant numerical challenges, a creep-damage algorithm was developed to account simultaneously for the progress of damage and visco-elastic processes in the concrete microstructure. The algorithm uses a time-adaptative scheme in which the instants at which damage occurs are explicitly searched for. This provides a non-local continuum damage procedure with very low sensitivity to the time or loading step. The proposed method is then used to simulate creep and restraint effects on radiation- induced degradation in concrete.

Keywords: irradiation, concrete, numerical model, meso-scale, creep, damage, radiation-induced volumetric swelling

1 Introduction

Potential applications for subsequent license renewal of the U.S. commercial nuclear power plants has modified the perspective of continuous operation beyond 60 years. Aging of non replaceable large components, such as the concrete containment building or the concrete biological shield (CBS), have become a focal point of attention. Among the varied concrete aging mechanisms under consideration, lacks of knowledge on irradiated concrete were identified (Graves et al., 2014).

Under neutron irradiation, concrete mechanical properties are affected by fluence exceeding $\approx 10^{19}$ n.cm^{-2} (Hilsdorf et al., 1978; Field et al., 2015). Radiation-induced volumetric expansion (RIVE) of aggregate appears as a first-order mechanism explaining irradiation damage of concrete (Seeberger and Hilsdorf, 1982; Field et al., 2015; Le Pape et al., 2015). Neutron high-attenuation, structural restrains and RIVE amplitude (order of magnitude 1%) result in elastic stresses in the CBS exceeding the strength of irradiated concrete (Le Pape, 2016). Two concurrent mechanisms can relax the developed stresses: damage, i.e., cracking, and viscous or quasi-viscous effects, i.e., creep. Irradiation experiments in test reactor are conducted at a rate of about 1 to 2 orders of magnitude higher than in light water reactors (LWRs), i.e., in actual commercial nuclear reactors (Maruyama et al., 2013; Remec et al., 2013). Because of the lack of experimental data at low irradiation flux, some rate effects and structural constraints are analyzed using numerical simulations at the microstructure level.

This raises the question of computing coupled creep and damage processes in a finite element software. The typical procedure consists in using finite differences to account for time-dependent processes (*i.e.* creep), and then Newton-Raphson iterations in-between the time steps to characterize the damage. This may lead to a strong sensitivity to the time or loading step as well as slow convergence rates. Furthermore, such staggered solving procedure assumes that there is a separation between the time scales of the two processes which is violated here. In the present paper, a numerical algorithm is presented to solve creep-damage problems in finite element codes. The algorithm finds *when* damage occurs, notably in the case when it occurs in-between the prescribed time steps. Therefore, the time-sensitivity is greatly reduced and the coupling between visco-elastic and damage processes is directly obtained through the algorithm. Also, the algorithm directly accounts in its formulation for time-dependent mechanical properties, which makes it particularly useful for the simulation of aging processes.

The algorithm is applied to the study of irradiated concrete, using a model previously validated (Giorla et al., 2015b) against literature data (Elleuch et al., 1972). Different test conditions are simulated in order to study the difference between short-term and long-term testing, as well as a preliminary investigation of the influence of external restraint on the irradiation-induced expansion and damage.

2 Damage algorithm

This section describes in details a time-adaptative algorithm to simulate the simultaneous progress of damage (using the framework of continuum damage mechanics) and visco-elastic processes. The present approach uses space-time finite elements to compute the time- and history-dependent response of quasi-brittle visco-elastic materials. While the idea of finite elements in space and time has been proposed as early as 1969 (Argyris and Scharpf, 1969; Fried et al., 1969), it is not until the 2000 that it received some attention in the context of solid mechanics (Idesman et al., 2001; Bajer and Dyniewicz, 2009; Dumont and Jourdan, 2012; Giorla et al., 2014), notably for their ability to represent spatial domains that undergo some change over time, like mechanical contact (Adélaide et al., 2003) or growth of expansive inclusions (Giorla et al., 2015a).

Space-time finite elements have several merits that make them preferable to more traditional approaches (finite elements in space combined with finite differences in time) in the context of viscoelastic quasi-brittle materials (Giorla et al., 2014):

- The time-stepping procedure is independent of the rheological model used for the visco-elastic material (for example generalized Maxwell or Kelvin-Voigt chains), while finite difference schemes must be written separately for each rheology.

- In space-time finite elements, the displacement field and its derivatives (strain, strain rate, stress, etc) are described as function of time, while with a finite difference scheme, they would be known at discrete instants only. The continuous variations of these fields allows to explicitly find *when* they reach critical values.

- There is a direct and simple relation between the length of the time step and space-time elementary matrices. Updating the time step has therefore a very low computational cost, while for finite difference schemes it necessitates to re-assemble the global system matrix and vector of nodal forces (e.g. Zienkiewicz et al. (1968)). This facilitates the use of time-step-adaptative strategies like the one presented here.

2.1 Description of the problem

The solid is considered as a visco-elastic material described by an arbitrary assembly of springs and dashpots and susceptible to continuum damage. The constitutive behavior is described with the following components:

- The displacement field $\mathbf{u}$ and several internal displacement fields $\mathbf{a}_j$. For a Maxwell or Kelvin-Voigt material, these internal displacement fields are the displacements associated with each dashpot in the model. ϵ and α_j are the strains derived from these displacement fields. In the following,

$\mathbf{x}$ denotes the concatenation of the displacement field and the internal displacement fields: $\mathbf{x} = [\mathbf{u}, ..., \mathbf{a}_j, ...]$

- A set of partial differential equations relating the stress σ to ϵ, the α_j, and their respective rates $\dot{\epsilon}$ and $\dot{\alpha}_j$. This set of partial differential equations can be written as a symmetric matrix for any spring-dashpot assembly (Biot, 1954). Examples for generalized Kelvin-Voigt, generalized Maxwell, and Burgers materials were given by the authors in (Giorla et al., 2014).

- A damage variable d which affects the different material properties of the constitutive equations defined above. In this paper, only the case of an isotropic scalar damage variable varying from 0 to 1 is considered, but the algorithm could be extended to other forms of damage or irreversible phenomena, including orthotropic damage or visco-plasticity.

- A failure criterion $\mathcal{C}$ which dictates at which strain or stress damage increases. In the general case, $\mathcal{C}$ can be written as a function of the extended displacements of the material $\mathbf{x}$, the damage variable d, and material parameters. Since all these variables vary in time, the criterion is also described as a function of time $\mathcal{C}(t)$. By convention, the failure surface is described by $\mathcal{C} = 0$, and the physically admissible domain by $\mathcal{C} \leq 0$. $\mathcal{C}$ must be a continuous and monotonic function of the displacements. A fully damaged element ($d = 1$) is considered always below its failure surface. The irreversibility conditions are summarized by:

$$\mathcal{C} \cdot \dot{d} = 0,\ \mathcal{C} \leq 0,\ \dot{d} \geq 0 \tag{1}$$

The following condition is also required, which is true for quasi-brittle materials without hardening:

$$\frac{\partial C}{\partial d} \leq 0 \tag{2}$$

- Finally, the solid is subject to external forces $\mathbf{f}_e$ on one section of its boundaries, imposed displacements $\hat{\mathbf{x}}$ on another, and internal body forces $\mathbf{f}_b$ (e.g. thermal expansion). The initial values of the displacement fields $\mathbf{x}(t = 0)$ are prescribed.

All fields are functions of space and time, including material properties like the stiffness or mechanical strength of the solid. The space-time coordinates (x, y, z, t) are omitted for clarity.

2.2 Space-time discretization

The solid is considered over a time interval $[t_S, t_F]$. In the following, $_S$ denotes the start of the time interval, $_F$ its finish, and Δt its length. The history of the system up to t_S is already known (either from the initial conditions or from the result of a previous time step).

The spatial domain is decomposed in a set of polygonal subdomains. The space-time finite element mesh is obtained by extruding each of these subdomains along the time direction between t_S and t_F. Each element has then two corresponding sets of nodes and shape functions, one set located at t_S and the second one at t_F, so that for each node in one set there is another node at the same spatial position in the other set.

The shape functions are taken as linear in time. This corresponds to the quasi-static approximation: acceleration effects are neglected.

Using this discretization, one can write a system of linear equations in the form of:

$$[\mathbb{K}(d) + \mathbb{L}(d, \Delta t)]\, \mathbf{x}_F = \mathbf{f}_F(d) - \mathbb{L}(d, \Delta t)\ \mathbf{x}_S \tag{3}$$

With $\mathbb{K}$ the assembled stiffness matrix, $\mathbb{L}$ the assembled viscosity matrix, $\mathbf{x}_S$ and $\mathbf{x}_F$ the vector of nodal displacements at t_S and t_F respectively, and $\mathbf{f}_F$ the vector of nodal forces at t_F.

The use of prismatic space-time elements ensures the following properties are true if the material properties are constant in time:

- $\mathbb{K}$ is independent of the time step.
- $\mathbb{L}$ is inversely proportional to the time step.

Proof is given in the appendix of (Giorla et al., 2014) and not repeated here for sake of brevity. The case of time-dependent material properties is addressed in section 2.6.

2.3 Damage algorithm

The system (3) is in principle non-linear. However, it is linear if d is set between $[t_S, t_F]$ for all elements, as in this case the material undergoes no increase of damage. A sequence of linear systems could then constructed by incrementing d using a step by step procedure similar to that proposed by Rots and Invernizzi (2004) or Zhu and Yvonnet (2015), accounting for the time dimension. Dunant et al. (2011) proposed a renormalisation which made such algorithm work when multiple materials are considered at once. The key difficulty is finding the instants at which damage should be incremented.

The algorithm is based on the fact that damage in an element can not increase before that element has reached its failure criterion $\mathcal{C}$. Since the solid is at equilibrium at the beginning of the time step, there is an interval after t_S during which damage does not increase. The goal of the algorithm is to find that interval and the next point of equilibrium. This is similar to the work of Dunant and Bentz (2015) which searches iteratively for these points of equilibrium. A proof of convergence of such algorithms is provided in the latter paper for quasistatic problems.

The algorithm adjusts the time step such that damage events occuring where $\mathcal{C}$ is reached happen at the beginning of the step. As opposed to other time-adjusting procedures, the current algorithm moves the *start* of the time step instead of the end to ensure damage occurs only when the elements reach their failure criteria, and not before.This is important as the algorithm ensures that the elements are all in a possible state at all times, making computing their viscous behavior correct.

The algorithm is described using the following steps. Figure 1 shows a flowchart of the entire procedure.

1. Initialization

The iterations are initialized with $t_0 = t_S$ and $\mathbf{x}_{S,0} = \mathbf{x}_S$. Damage is assumed constant during the time step and equal to its value at the beginning of the time step: $d_0 = d_S$.

2. Resolution

t_i, $\mathbf{x}_{S,i}$ and d_i are known and such that all elements at t_i are strictly below their failure surface ($\mathcal{C}(t_i) < 0$ in all elements), and a system similar to (3) has been built. Resolution of that system gives the displacements at the end of the time step $\mathbf{x}_{F,i}$.

3. Failure criterion

From $\mathbf{x}_{S,i}$, $\mathbf{x}_{F,i}$, d_i and the space-time shape functions, the failure criteria for all elements can be calculated as a function of space and time. Notably, for all elements the first instant at which their failure criterion is reached can be obtained. This can be directly evaluated for simple criteria (constant strength or limit strain), but may necessitate a bisection over time in the general case.

4. Damage increment

t_{i+1} is the first instant at which an element $\mathcal{E}$ reaches its failure criterion. Condition (2) ensures that $t_{i+1} > t_i$ by continuity. The damage in $\mathcal{E}$ is then increased at t_{i+1} by an fixed amount δd. This action must be repeated until $\mathcal{E}$ is strictly below than its failure surface at t_{i+1}. This defines d_{i+1}.

5. Time step adjustment

The irreversibility conditions (1) are satisfied over the interval $[t_i, t_{i+1}]$, so the solution calculated at step *2.* gives the actual solution of the problem on that interval and does not need to be calculated again. Therefore, the next time step is $[t_{i+1}, t_F]$. This can be achieved by moving all nodes located at t_i to t_{i+1}.

$\mathbf{x}_{S,i+1}$ is obtained as the values of the extended displacements at t_{i+1} from $\mathbf{x}_{S,i}$, $\mathbf{x}_{F,i}$, and the space-time finite element shape functions. $\mathbb{K}$ and is not affected, and $\mathbb{L}$ must be scaled according to that new time interval. Finally, the elementary contributions of the damaged element $\mathcal{E}$ to $\mathbb{K}$, $\mathbb{L}$ and $\mathbf{f}$ must be re-evaluated. This yields a new assembled system with the same structure as (3).

6. Iteration

Go back to *2.* using the new t_{i+1}, $\mathbf{x}_{S,i+1}$ and d_{i+1}.

7. Exit

The algorithm has converged when no element reaches its failure surface before t_F (step *3.*). This always occurs after a finite number of iterations due to the fixed damage increment δd.

2.4 Non-locality

The damage pattern obtained from a given stress-strain relationship depends strongly on the mesh if the relationship has been defined from the local stress and strain of the elements. This in turns means that given a domain and boundary conditions, the energy dissipated by the initiation and propagation of damage is not constant with the mesh. Problematically, this energy converges to 0 as the mesh is refined as the elements damaged coalesce into a single band of vanishing width. To palliate this defect, Pijaudier-Cabot and Bazant (1987) proposed to transform the formulation of the stress-strain relationship from a local to a non-local one.

To make the proposed algorithm non-local, the strains are smoothed using a kernel of radius r_{nl} when calculating the failure criterion $\mathcal{C}$. The radius is characteristic of the size of the fracture process zone, a consequence of the underlying microstructure of the material. For example, the characteristic distance for concrete models is frequently taken as 1 to 2 times the largest aggregate diameter. This corresponds to the width of observed networks of microcracks forming around a main crack when the concrete is failing in tension (Otsuka and Date, 2000).

The variable to be smoothed can in principle be chosen freely. However, in practice, it is preferable to smooth strains, as these are defined independently of the material properties and can therefore be meaningfully scaled and added (Jirásek, 1998). The internal strain fields associated with the dashpots are also smoothed using the same kernel as they represent a certain fraction of the strain history of the material. The stresses are then evaluated using the non-local strains and the local mechanical properties.

The equilibrium problem solved is local, but the failure criterion is non-local. This is physically explained by t Smoothing the failure criterion ensures that damage forms over the prescribed radius. Figure 2 shows the damage pattern obtained for a plate subject to uni-axial tension for different mesh sizes. The material is a generalized Kelvin-Voigt chain with one module, with a linear-softening strain-stress relation. The width of the damage band is independent of the characteristic size of the elements in the mesh.

This procedure is numerically more efficient than solving the complete non-local problem by introducing the smoothing couplings in the system of equations. Indeed, we find that only the criterion needs to be non-local using the solving strategy described in this paper. Nonetheless, the problem is discretized not only in space but also in time, and the sensitivity to this latter discretisation should also be assessed.

2.5 Time-step sensitivity

The algorithm is adaptative in time and is not affected by the prescribed the time (or load) step. This property is shown on a simple case with a single square element on which a tensile displacement is applied at a constant rate. The material is the same as the one used in the previous test case, with a stress-strain curve presenting a linear softening branch. The time step is varied between 0.001 and 0.5 in arbitrary units, with the larger time step chosen so that the first step occurs beyond the peak. The resulting stress-strain curves with the different time steps are shown in Figure 3. For all time steps, the algorithm gives as a result the exact behavior of the element for the considered strain. Furthermore, the damage algorithm (not shown in the graph) always finds the exact peak of the material behavior and initiates damage at this time. This illustrates the robustness of the algorithm to large time (or load) steps.

Of course, when the material has a time-dependent behavior, the time steps must be chosen to be able to capture it.

2.6 Time-dependent material properties

The algorithm remains valid with little modifications when the material properties are function of time, due to (for example) ageing, irradiation or temperature effects.

- $\mathbb{K}$ only depends on the elastic properties at t_F as it is a representation of the instantaneous response of the material.

- $\mathbb{L}$ depends on the rate of the viscous properties. However, it can be divided into two parts: the first is inversely proportional to the time step, and independent of the rate of the viscous properties, while the second is independent of the time step and depends only on the rate of the viscous properties. The two parts can be stored independently in the memory in the memory so that the adjustment of $\mathbb{L}$ with the time step remains simple.

- If the strength (or limit strains) of the material are time-dependent, the algorithm can also be used as written. In this case, the failure criterion becomes a more elaborate function of time but retains its continuity properties. Therefore, the instant at which an element reaches its failure criterion can still be obtained with an appropriate bisection, by evaluating $\mathcal{C}$ at different instants.

2.7 Matrix conditioning

Since $\mathbb{L}$ is inversely proportional to the time step and $\mathbb{K}$ is constant, the conditioning number of the final assembled matrix $\mathbb{K}+\mathbb{L}$ increases when the time step decreases. Therefore, resolution of (3) with a conjugate gradient solver becomes increasingly difficult after each iteration of the damage algorithm (Gilbert and Nocedal, 1992). However, when the time step $(f_F - t_i)$ becomes much smaller than the characteristic time of the viscoelastic processes, the problem may be considered as "instantaneous" and rate effects neglected.

When this occurs, the viscoelastic variables $\mathbf{a}_j$ can be fixed to their last computed values, leaving only the displacements $\mathbf{u}$ as unknown in (3). The contribution of $\mathbb{L}$ to the global system then vanishes, unless the material behavior depends explicitly on the strain rate $\dot{\epsilon}$ (this would be the case, for example, of a single Kelvin-Voigt unit). This approximation greatly improves the conditioning number of the global system matrix for very small time steps, and therefore improves the resolution of (3).

In the present work, this threshold is taken equal to 1 second.

3 Application to irradiated concrete

The algorithm is applied to meso-scale simulations of concrete specimens subject to irradiation-induced expansion and degradation. Concrete is represented at its meso-level with aggregates embedded in a cement paste matrix. The simulations are carried out in two dimensions using plane strain assumption to limit the computational time. The model, previously validated in (Giorla et al., 2015b) on irradiation experiments from the literature (Elleuch et al., 1972), is briefly summarized here.

3.1 Microstructure

The aggregates are generated as random polygons following the work of Beddow and Meloy (1980). The polar radius r of each vertex is calculated as an harmonic function of the polar angle θ and the average radius of the particle r_0:

$$r = r_0 \left[1 + \sum_{j=1}^{m} e^{-p\log(j)-b} \cos(j\theta + \alpha_j) \right] \tag{4}$$

With p and b parameters describing the shape of the particles, and α_j random numbers uniformly taken between 0 and 2π. p and b are taken equal to 0.9 and 1.9 respectively from the work of Wang et al. (1999), while the radii are generated using a Fuller and Thompson (1907) curve between 8 and 0.5 mm. The number of vertexes in each aggregate is randomly taken between 6 and 10. Only the largest aggregates are represented; the cement paste mechanical properties are increased to account for the missing aggregate fraction.

The aggregates are randomly placed (from the largest to the smallest) in a 10×10 cm sample with a minimum interdistance of 0.5 mm. The sample is then meshed with a conforming Delaunay triangulation so that the node density is relatively constant throughout the sample. The relative size of the sample and the aggregates were chosen so that the microstructure was representative of the material, and avoid the variability induced by the presence of unusually large aggregates as observed in a previous works (Giorla et al., 2015b).

The microstructure and a detail of the finite element mesh is shown in Figure 4. The mesh is composed of 19,174 linear elements, for a computational time ranging between 24 and 48 hours.

3.2 Constitutive behaviors

In the following, $_p$ denotes properties of the cement paste, and $_a$ the aggregates.

Cement paste

Cement paste is simulated as a viscoelastic quai-brittle damage material with thermal deformation. Creep is simulated with an aging logarithmic model assuming a separation of the short-term recoverable creep ϵ_r and the long-term non-recoverable creep ϵ_c. The rheological model is thus composed by an elastic spring in series with a Kelvin-Voigt unit (short-term creep) and a time-dependent dashpot (long-term creep) as with the B3 model (Bažant and Baweja, 2000) or the model more recently proposed by Hilaire et al. (2014). This assembly is shown in Figure 5.

The corresponding set of constitutive differential equations is:

$$\sigma = (1-d)\ \mathbb{C}_e : [\epsilon - \epsilon_r - \epsilon_c - \epsilon_{imp}] \tag{5}$$

$$\sigma = (1-d)\ [\mathbb{C}_r : \epsilon_r + \mathbb{E}_r : \dot{\epsilon}_r] \tag{6}$$

$$\sigma = (1-d)\ \left[1 + \frac{t}{\tau_c}\right] \mathbb{E}_c : \dot{\epsilon}_c \tag{7}$$

With $\mathbb{C}_e$ the elastic stiffness tensor of the material, $\mathbb{C}_r$ and $\mathbb{E}_r$ the stiffness and viscosity tensors of the Kelvin-Voigt module, $\mathbb{E}_c$ the initial viscosity tensor of the time-dependent dashpot, ϵ_{imp} the imposed deformation (shrinkage, thermal strains, etc), and τ_c the characteristic time of the logarithmic creep. This system can be made symmetric by substracting the elastic equation (5) to each viscous relation (6-7).

To limit the number of calibration parameters, the different creep properties are assumed equal: $\tau_c\ \mathbb{C}_r = \mathbb{E}_r = \mathbb{E}_c$. Also, the Poisson ratio of all springs and dashpots are constants and equal, following experimental observations on biaxial long-term creep tests by Charpin et al. (2015).

The cement paste is assumed to fail only in tension. The failure criterion $\mathcal{C}_p$ is written so that the material exhibits a linear softening branch after the peak:

$$\mathcal{C}_p = \|\bar{\epsilon}\| - \frac{\mathrm{E}_{soft}}{\mathrm{E}_{soft} + \mathrm{E}_{inst}} \epsilon_{y,t} \tag{8}$$

With $\|\bar{\epsilon}\|$ the maximum principal component of the averaged (non-local) strains, E_{soft} the slope of the softening branch (a material parameter), E_{inst} the current instantaneous modulus, accounting for the damage and the evolution of the creep processes, and $\epsilon_{y,t}$ the strain at the end of the softening branch. In practice, E_{soft} is obtained from the tensile strain at the peak ϵ_t, the tensile strain at the end of the softening branch $\epsilon_{y,t}$, and the Young modulus of the material E.

Aggregates

The aggregates mechanical behavior is taken as a purely elastic and made of homogeneous phases undergoing the same RIVE. The strain ϵ_Φ imposed by the irradiation-induced swelling is given as a function of the neutron fluence Φ by Zubov and Ivanov (1966) equation:

$$\epsilon_\Phi = \frac{\kappa \; \epsilon_{max} \left(e^{\delta\Phi} - 1\right)}{\epsilon_{max} + \kappa \; e^{\delta\Phi}} \tag{9}$$

With ϵ_{max} the final deformation, and κ and δ two parameters controlling the shape of the sigmoid curve.

Cracking of aggregates is neglected as it is expected that the much less resistant cement paste will fail first. This hypothesis will be verified a posteriori by measuring the stresses in the aggregates.

3.3 Material properties

The mechanical properties, given in Table 1, are chosen to represent a prototypical concrete used for the construction of nuclear power plants in the 70s. In order to provide a basis of comparison, the mechanical properties of the cement paste and the aggregates are calibrated so that the elastic and strength macroscopic properties of the sample are similar to the one used by Le Pape (2016) for a structural analysis of a biological shield (Young's modulus E = 34 GPa, compressive strength $f_c = 40$ MPa).

The creep properties are provided by the analysis of uniaxial creep experiments on pure cement paste samples by Le Roy (1995) (water/cement ratio 0.5). The Poisson ratio is assumed to be constant in time. The creep properties are adjusted with the temperature using an Arrhenius-type law. The activation energy E_{act} is taken equal to 5000 K according the recommendations of Bažant and Baweja (2000).

Thermal deformations are accounted for using the thermal expansion coefficients θ_p and θ_a from the radiation experiments of Elleuch et al. (1972). Shrinkage is neglected as the effect of irradiation is not well understood yet.

Table 1: Material properties for the cement paste and the aggregates. (1) back-calculated using the target Young's modulus and compressive strength; (2) typical value for concrete; (3) calibrated on the creep experiments of cement pastes with a water-cement ratio of 0.5 of Le Roy (1995); (4) arbitrary parameter; (5) from the experimental data of Elleuch et al. (1972).

Cement paste				
Elastic properties	E_p	20	[GPa]	(1)
	ν_p	0.2	[-]	(2)
Creep properties	η_c	40	[GPa.d]	(3)
	τ_c	2	[d]	(3)
	E_{act}	5000	[K]	(2)
Failure properties	ϵ_t	0.4	[mm/m]	(1)
	$\epsilon_{y,t}$	0.5	[mm/m]	(1)
	r_{nl}	0.5	[mm]	(1)
	δd	0.1	[-]	(4)
Thermal properties	θ_p	9	[10^{-6} 1/K]	(5)
Aggregates				
Elastic properties	E_a	60	[GPa]	(2)
	ν_a	0.2	[-]	(2)
Thermal properties	θ_a	7.5	[10^{-6} 1/K]	(5)

3.4 Test conditions

The model is tested in 8 different conditions in order to assess the relevance of creep in the analysis of irradiation-induced damage. The conditions are the combination of three different factors:

- With/Without creep. For the simulation without creep, the differential equations (6-7) are ignored and ϵ_c and ϵ_r are both set to 0. Otherwise, the same numerical procedure is adopted.
- Slow/Fast irradiation. The neutron fluence is taken as a linear function of time up to 4×10^{19} n/cm^2. The fluxes are chosen to represent fast-flux experiments in test reactors (duration of irradiation 47 days) of pressurized water reactors operation (duration 80 years) respectively.
- Free/Restrained. In the later case, the vertical displacements of the bottom and top edges of the sample are blocked, but the sample is still free to deform in the horizontal direction. In both cases the middle point of the bottom edge is fixed to avoid global displacement of the sample.

The temperature is supposed homogeneous throughout the sample and equal to 65 °C which is the design operating conditions in commercial test reactors (Field et al., 2015). Effect of irradiation on relative humidity is neglected due to lack of supporting data.

4 Results and Discussion

The expansions and average damage in the cement paste were calculated at each step of the simulations. The values of the expansions correspond to maximum displacement variation between two opposite edges of the sample, as if they were measured with an external extensometer or a micrometer. Damage is obtained as the average of the damage scalar d over the elements representing the cement paste. Note that in Fig. 6-9, the marks (circles) correspond to the actual simulation results, while the curves are obtained using the `loess` smoothing function from the R statistical software package (R Core Team, 2012).

Figure 6 shows the respective evolutions of concrete volume increase as a function of the neutron fluence for all studied cases.

When unrestrained, the expansion is isotropic and its evolution with fluence is identical for the four studied cases (underlying grey curve) This result was expected as the RIVE imposes an elastic deformation to the aggregates which does not depend on the neutron flux.

When restrained, the expansion can only develop laterally. The vertically-restrained RIVE results in the creation of significant stresses, which, in turn, cause the development of creep. Creep presents a significant effect on the evolution of the volumetric expansion and internal damage. An important and sudden deformation increase is observed corresponding to the formation and opening of a compressive fracture through the sample. When creep is considered, the development of this fracture occurs at a higher fluence and in a more progressive manner. Once this fracture opened, the remaining of the microstructure produces a micro-cracking pattern similar to that developed in unrestrained conditions. During this later phase, the volume increases at a similar rate for all cases, although the rates and amplitudes appear smaller when expansion is restrained. Creep increases the expansion during this later stage by an amount that seems to be higher for low-flux irradiation.

The damage as a function of the neutron fluence is plotted, respectively, in Figure 7 for the unrestrained condition and Figure 8 for the restrained case. The damage evolutions in the simulations neglecting creep are similar regardless of the time scale of the irradiation, i.e., slow or fast flux, which demonstrates the stability of the damage algorithm. At a given fluence level, creep contributes to the reduction of average damage. It appears that creep causes a latency effect on the initiation of damage. This latency effect, i.e., apparent shift in fluence, decreases with the neutron flux because lower flux permits the relaxation through a viscoelastic process. This observation illustrates the competition between the two mechanical energy dissipation playing a role in the stress relaxation: the formation of cracks and the viscous relaxation. Notably, in the restrained case accounting for creep effects, the initiation and propagation of damage is much smoother, and vertical cracks can be observed in the sample.

Finally, Figure 9 shows the volume increase as a function of the damage for the restrained case. The results of the simulations in the unrestrained case are plotted in grey solid lines. When creep is considered, the material exhibits a much larger expansion for the same degree of damage for a long-term irradiation exposure. This also indicates that for the long-term scenario, damage in the material would be much lower for the same level of expansion when calculated with creep than what would be obtained with a purely elastic simulation. This indicates a strong need for accounting for visco-elastic effects in the analysis of the long-term durability of CBS.

4.1 Creep of Irradiated Cement Paste and Concrete

The current model assumes that the creep properties of the material remains unaffected by irradiation. This is a rather simplistic approximation which is dictated by the poor understanding of the effects of irradiation on shrinkage and creep: (1) The mechanistic understanding of unirradiated creep is still controversial despite decades of research, and, (2) Very limited data on shrinkage and creep of irradiated cementitious materials are available in the literature (Gray, 1971; McDowall, 1971).

Under gamma irradiation for 10 months at a dose of 0.114 $\mathrm{kGy\,h^{-1}}$, McDowall (1971) found that the creep rate of concrete (10 MPa) decreases while the shrinkage rate is increased. The specimens were sealed in copper foils, although venting radiolytic gas is permitted through a gas bubbler filled with water. While moisture transport through vapor diffusion is not allowed, gas transport could lead to a partial, though limited, 'drying' of the specimens. Hence, it can be assumed, by lack of better data, that the effects on creep and shrinkage rates are primarily attributed to gamma-ray exposure.

Gamma irradiation induced hydrogen production of absorbed water and nano-confined water are respectively two and one order(s) of magnitude higher than that of bulk water in controlled-nanopore (8-300 nm) boro-silicate glasses (Rotureau et al., 2005; Le Caër et al., 2005). The microstructure of calcium-silicate hydrates (C-S-H) suggests that similar radiolytic effects could be observed in cement pastes potentially causing change primarily at the nanoscale. A possible irradiation-induced drying mechanism of absorbed and nano-confined water could result in the collapse of C-S-H as it is observed after drying under sustained moderate temperature (Jennings et al., 2007; Maruyama et al., 2014). Hence, such a mechanism could possibly cause the increase of the apparent viscosity, and thus, the decrease of the creep rate under gamma irradiation. Concurrently, radiolysis of absorbed water at the C-S-H surface can result in releasing the disjoining pressure (Beltzung and Wittmann, 2005), and hence, increasing the shrinkage rate.

Under concurrent neutron and gamma irradiation, shrinkage and, subsequently, creep (6.9 MPa) of Portland cement grout specimens were tested by Gray (1971) at varied temperatures ranging from 20 °C to nearly 95 °C. For about 15 d, the creep specimens were subjected to irradiation in Herald test reactor (UK). Fast neutron fluence is not specifically reported but can be estimated at $\approx 0.75 \times 10^{19}$ n.cm^{-2} with a flux of $\approx 5 \times 10^{12}$ n.cm^{-2}s^{-1}. The deformation history reconstructed from Gray's data is presented in Figure 10. Creep kinetics at 60 to 95 °C (average $\approx$ 70 °C) under concurrent irradiation is one order of magnitude higher than creep of specimens out-of-pile before or after irradiation in a similar range of temperature. The relative humidity and loss of mass of the specimens were not monitored. Neutron-induced radiolytic effects on water are similar in nature to gamma ray effects (Kontani et al., 2010), and thus, should lead to a decrease of the creep rate following the observation of McDowall. This indicates the possibility of an additional mechanism, even though experimental data support that neutron irradiation has a limited effect on the macroscopic mechanical properties on cement paste (Gray, 1971; Elleuch et al., 1972). The possible mechanisms of neutron-induced damage on the solid phase of cement hydrates remain poorly understood and requires further investigation.

4.2 On the Role of Temperature

The effects of temperature were not specifically studied in this article but need to be discussed as an additional source of discrepancy between test reactor data obtained at 40 to 250 °C and the actual behavior of concrete in LWRs at $<$ 65 °C. In addition to the known effects of temperature (Naus, 2010), specific interactions between temperature and irradiation exist: (1) Dehydration caused by combined drying and radiolysis results in important shrinkage strains in the cement paste (Elleuch et al., 1972). (2) Thermal expansion aggravate the RIVE of aggregate leading to the development of cracks in the paste (Le Pape et al., 2015). (3) Temperature increase allows the annealing of neutron-irradiation-induced point defects. Hence, RIVE rate is higher at lower temperature (Bylov et al., 1981). These effects are not accounted for in the present model and require further research.

5 Conclusion

A numerical algorithm was presented in this paper to compute creep and continuum damage with space-time finite elements. The algorithm adapts the length of the time step to the rate of the damage process, thus allowing an accurate characterization of the viscoelastic dissipation in the material. This decreases greatly the sensitivity of the procedure to the time or loading step, even when the material is directly loaded after its peak in the stress-strain curve. The method is non-local by considering average strains during the evaluation of the instant at which failure occurs.

The algorithm was applied to the study of radiation-induced expansion and degradation. Concrete was simulated at the meso-scale with aggregates represented by polygonal inclusions embedded in a cementitious matrix. The expansion was driven by the radiation-induced swelling of the aggregates, while the damage propagated in the viscoelastic cement paste. Different scenarios were evaluated to investigate the rate and restraint effects on the overall expansion and damage. Imposing a restraint on the expansion causes an increase of the deformation in the lateral direction, and fracture formation was observed through the sample during the early stages of the irradiation. However, accounting for creep in the simulation reduces the damage onset and propagation for the same level of expansion. The final volumetric expansion rate as a function of the fluence seemed independent of the conditions and rate of irradiation. These results are of practical interest for the interpretation of irradiation experiments conducted in test reactor, i.e., fast flux and unrestrained expansion, in the perspective of analyzing the effects of neutron irradiation on the concrete biological shield in actual light water reactors (LWRs) conditions. In other words, the obtained results suggest that creep can play a favorable role in terms of LWRs long-term operation by delaying the initiation of damage to a higher fluence exposure.

Still, several questions remain open on the effects of radiation on creep, including the role of gamma radiation, as well as the strong coupling with temperature. Confirmatory experimental results complementing those obtained by McDowall (1971) and Gray (1971) are required to better understand interactions between creep and radiation-induced swelling and damage in concrete. The proposed algorithm can serve as a numeric tool to carry out this analysis at the concrete mesoscale and formulate a more complete material model. A set of probabilistic simulations could then be performed with varying conditions in order to express a numerical macroscopic model that could be used in a structural analysis.

The algorithm itself has a generic and highly flexible formulation, which makes it suitable for the analysis of several creep-degradation phenomena in concrete. It was used in previous publications in the context of alkali-silica reaction (Giorla et al., 2015a), radiation-induced volumetric expansion (Giorla et al., 2015b), or snap-back analysis of visco-elastic materials (Dunant and Hilaire, 2015). It could be applied to analyze early-age cracking, loading rate effects on concrete failure, or other long-term durability phenomena such as delayed ettringite formation.

6 Acknowledgements

This research is sponsored by the U.S. Department of Energy (DOE) Light Water Reactor Sustainability Program. This manuscript has been authored by UT-Battelle, LLC under Contract No. DE-AC05-00OR22725 with the U.S. Department of Energy. The United States Government retains and the publisher, by accepting the article for publication, acknowledges that the United States Government retains a non-exclusive, paid-up, irrevocable, world-wide license to

publish or reproduce the published form of this manuscript, or allow others to do so, for United States Government purposes. The Department of Energy will provide public access to these results of federally sponsored research in accordance with the DOE Public Access Plan (`http://energy.gov/downloads/doe-public-access-plan`).

7 Notations

The following symbols are used in this paper:

$\mathbf{a}_j$ = internal viscous displacement of the dashpots of the material
b = parameter controlling the shape of the aggregate particles (4)
$\mathbb{C}$ = fourth-order elastic stiffness tensor
$\mathcal{C}$ = failure criterion (8)
d = scalar damage variable
$\mathbb{E}$ = fourth-order viscosity tensor
E = elastic Young's modulus
E_{act} = activation temperature of the Arrhenius law for creep
$\mathbf{f}$ = forces applied on the system
$\mathbb{K}$ = global assembled stiffness matrix (3)
$\mathbb{L}$ = global assembled viscosity matrix (3)
p = parameter controlling the shape of the aggregate particles (4)
r = radius of the aggregate particles (4)
r_{nl} = radius of the non-local averaging
t_F = time at the end of the time step
t_S = time at the start of the time step
$\mathbf{u}$ = displacement field
$\mathbf{x}$ = global unknown of the problem (3)
α_j = second-order internal viscous strain tensors, deriving from $\mathbf{a}_j$
Δt = time step
δ = scale parameter for the Zubov and Ivanov curve (9)
ϵ = second-order strain tensor, deriving from $\mathbf{u}$

ϵ_{max} = amplitude of the RIVE (9)

ϵ_t = limit strain at the peak of the stress-strain curve (8)

$\epsilon_{y,t}$ = limit strain at the end of the softening curve (8)

η = uni-axial viscosity

θ = thermal expansion coefficient

κ = shape parameter for the Zubov and Ivanov curve (9)

ν = Poisson ratio

σ = second-order stress tensor

τ_c = characteristic time of the logarithmic creep

ϕ = neutron fluence (9)

References

Adélaide, L., Jourdan, F., Bohatier, C., 2003. Frictional contact solver and mesh adaptation in space–time finite element method. European Journal of Mechanics-A/Solids 22, 633–647.

Argyris, J., Scharpf, D., 1969. Finite elements in time and space. Nuclear Engineering and Design 10, 456–464.

Bajer, C., Dyniewicz, B., 2009. Virtual functions of the space–time finite element method in moving mass problems. Computers & Structures 87, 444–455.

Bažant, Z., Baweja, S., 2000. Creep and shrinkage prediction model for analysis and design of concrete structures: Model B3. ACI Special Publications 194, 1–84.

Beddow, J., Meloy, T., 1980. Testing and characterization of powders and fine particles.

Beltzung, F., Wittmann, F., 2005. Role of disjoining pressure in cement based materials. Cement and Concrete Research 35, 2364–2370.

Biot, M., 1954. Theory of stress-strain relations in anisotropic viscoelasticity and relaxation phenomena. Journal of Applied Physics 25, 1385–1391.

Bylov, V., Denisov, A., Dubrovskii, V., Korenevskii, V., Krivokoneva, G., Muzalevskii, L., 1981. Effect of irradiation temperature on the radiation expansion of quartz. Atomnaya Energiya 51, 593–595.

Charpin, L., Le Pape, Y., Coustabeau, E., Masson, B., Montalvo, J., 2015. EDF study of 10-years concrete creep under unidirectional and biaxial loading: evolution of Poisson coefficient under sealed and unsealed conditions, in: Proceedings of CONCREEP 10, pp. 1381–1390.

Dumont, S., Jourdan, F., 2012. A space-time finite element method for elastodynamics problems with a moving loading zone, in: Proceedings of the Eleventh International Conference on Computational Structures Technology.

Dunant, C., Bentz, E., 2015. Algorithmically imposed thermodynamic compliance for material models in mechanical simulations using the aim method. International Journal for Numerical Methods in Engineering .

Dunant, C., Hilaire, A., 2015. Fully-coupled creep-damage models for concrete, in: Proceedings of CONCREEP 10, pp. 1603–1610.

Dunant, C.F., Bordas, S.P., Kerfriden, P., Scrivener, K.L., Rabczuk, T., 2011. An algorithm to compute damage from load in composites. Frontiers of Architecture and Civil Engineering in China 5, 180–193.

Elleuch, L., Dubois, F., Rappeneau, J., 1972. Effects of neutron radiation on special concretes and their components. Special Publication of The American Concrete Institute 43, 1071–1108.

Field, K., Remec, I., Le Pape, Y., 2015. Radiation Effects on Concrete for

Nuclear Power Plants, Part I: Quantification of Radiation Exposure and Radiation Effects. Nuclear Engineering and Design 282, 126–143.

Fried, I., Cremer, M.A., McMurtry, P.A., 1969. Finite-element analysis of time-dependent phenomena. AIAA Journal 7, 1170–1173.

Fuller, W., Thompson, S., 1907. The laws of proportioning concrete. Journal of Transportation Division, American Society of Civil Engineers 59, 67–143.

Gilbert, J., Nocedal, J., 1992. Global convergence properties of conjugate gradient methods for optimization. SIAM Journal on optimization 2, 21–42.

Giorla, A., Scrivener, K., Dunant, C., 2014. Finite elements in space and time for the analysis of generalised visco-elastic materials. International Journal for Numerical Methods in Engineering 97, 454–472.

Giorla, A., Scrivener, K., Dunant, C., 2015a. Influence of visco-elasticity on the stress development induced by alkali–silica reaction. Cement and Concrete Research 70, 1–8.

Giorla, A., Vaitovà, M., Le Pape, Y., Ŝtemberk, P., 2015b. Meso-scale modeling of irradiated concrete in test reactor. Nuclear Engineering and Design 295, 59–73.

Graves, H., Le Pape, Y., Naus, D., Rashid, J., Saouma, V., Sheikh, A., Wall, J., 2014. Expanded Material Degradation Assessment (EMDA), Volume 4: Aging of Concrete. Technical Report NUREG/CR-7153, ORNL/TM-2011/545. U.S. Nuclear Regulatory Commission.

Gray, B., 1971. The effects of reactor radiation on cement and concrete, in: Proceedings of an Information Exchange Meeting on 'Results of Concrete Irradiation Programmes', Commission des Communautés Européennes, Brussels, Belgium. pp. 17–39.

Hilaire, A., Benboudjema, F., Darquennes, A., Berthaud, Y., Nahas, G., 2014. Modeling basic creep in concrete at early-age under compressive and tensile loading. Nuclear Engineering and Design 269, 222–230.

Hilsdorf, H., Kropp, J., Koch, H., 1978. The effects of nuclear radiation on the mechanical properties of concrete. Special Publication of The American Concrete Institute 55, 223–254.

Idesman, A., Niekamp, R., Stein, E., 2001. Finite elements in space and time for generalized viscoelastic maxwell model. Computational Mechanics 27, 49–60.

Jennings, H.M., Thomas, J.J., Gevrenov, J.S., Constantinides, G., Ulm, F.J., 2007. A multi-technique investigation of the nanoporosity of cement paste. Cement and Concrete Research 37, 329–336.

Jirásek, M., 1998. Nonlocal models for damage and fracture: comparison of approaches. International Journal of Solids and Structures 35, 4133–4145.

Kontani, O., Ichikawa, Y., Ishizawa, A., Takizawa, M., Sato, O., 2010. Irradiation effects on concrete structure, in: International Symposium on the Ageing Management and Maintenance of Nuclear Power Plants, pp. 173–182.

Le Caër, S., Rotureau, P., Brunet, F., Charpentier, T., Blain, G., Renault, J., Mialocq, J., 2005. Radiolysis of confined water: Hydrogen production at a high dose rate. ChemPhysChem 6, 2585–2596.

Le Pape, Y., 2016. Structural effects of radiation-induced volumetric expansion on unreinforced concrete biological shields. submitted to Nuclear Engineering and Design .

Le Pape, Y., Field, K., Remec, I., 2015. Radiation Effects in Concrete for Nuclear Power Plants - Part II: Perspective from Micromechanical Modeling. Nuclear Engineering and Design 282, 144–157.

Le Roy, R., 1995. Déformations instantanées et différées des bétons à hautes performances. Ph.D. thesis. École Nationale des Ponts et Chaussées.

Maruyama, I., Kontani, O., Sawada, S., Sato, O., Igarashi, G., Takizawa, M., 2013. Evaluation of irradiation effects on concrete structure - Background and preparation of neutron irradiation test, in: Proceedings of the ASME 2013 Power Conference POWER2013, Boston MA, USA.

Maruyama, I., Nishioka, Y., Igarashi, G., Matsui, K., 2014. Microstructural and bulk property changes in hardened cement paste during the first drying process. Cement and Concrete Research 58, 20–34.

McDowall, D., 1971. The effect of gamma irradiation on the creep properties of concrete, in: Proceedings of an Information Exchange Meeting on Results of Concrete Irradiation Programmes, Commission of the European Communities. pp. 55–69.

Naus, D., 2010. A Compilation of Elevated Temperature Concrete Material Property Data and Information for Use in Assessments of Nuclear Power Plant Reinforced Concrete Structures. US Nuclear Regulatory Commission, Office of Nuclear Regulatory Research.

Otsuka, K., Date, H., 2000. Fracture process zone in concrete tension specimen. Engineering Fracture Mechanics 65, 111–131.

Pijaudier-Cabot, G., Bazant, Z.P., 1987. Nonlocal damage theory. Journal of Engineering Mechanics 113, 1512–1533.

R Core Team, 2012. R: A Language and Environment for Statistical Computing. R Foundation for Statistical Computing. Vienna, Austria. URL: `http://www.R-project.org/`. ISBN 3-900051-07-0.

Remec, I., Field, K., Naus, D., Rosseel, T., Busby, J., 2013. Concrete aging and degradation in NPPs: LWRS program R&D progress report, in: 2013 ANS Winter Meeting and Nuclear Technology Expo, Washington, D.C.

Rots, J., Invernizzi, S., 2004. Regularized sequentially linear saw-tooth softening model. International Journal for Numerical and Analytical Methods in Geomechanics 28, 821–856.

Rotureau, P., Renault, J.P., Lebeau, B., Patarin, J., Mialocq, J.C., 2005. Radiolysis of confined water: Molecular hydrogen formation. ChemPhysChem 6, 1316–1323.

Seeberger, J., Hilsdorf, H., 1982. Einfluss von Radioaktiver Strahlung auf die Festigkeit und Struktur von Beton. Technical Report NR2505. Institüt fur Massiubau und Baustofftechnologie, Arbeitlung Baustofftechnologie, Universität Karlsruhe, Germany.

Wang, Z., Kwan, A., Chan, H., 1999. Mesoscopic study of concrete i: generation of random aggregate structure and finite element mesh. Computers & Structures 70, 533–544.

Zhu, Q.Z., Yvonnet, J., 2015. An incremental–iterative method for modeling damage evolution in voxel-based microstructure models. Computational Mechanics 55, 371–382.

Zienkiewicz, O., Watson, M., King, I., 1968. A numerical method of visco-elastic stress analysis. International Journal of Mechanical Sciences 10, 807–827.

Zubov, V., Ivanov, A., 1966. Expansion of quartz caused by irradiation with fast neutrons. Soviet Physics Crystallography 11, 372–374.

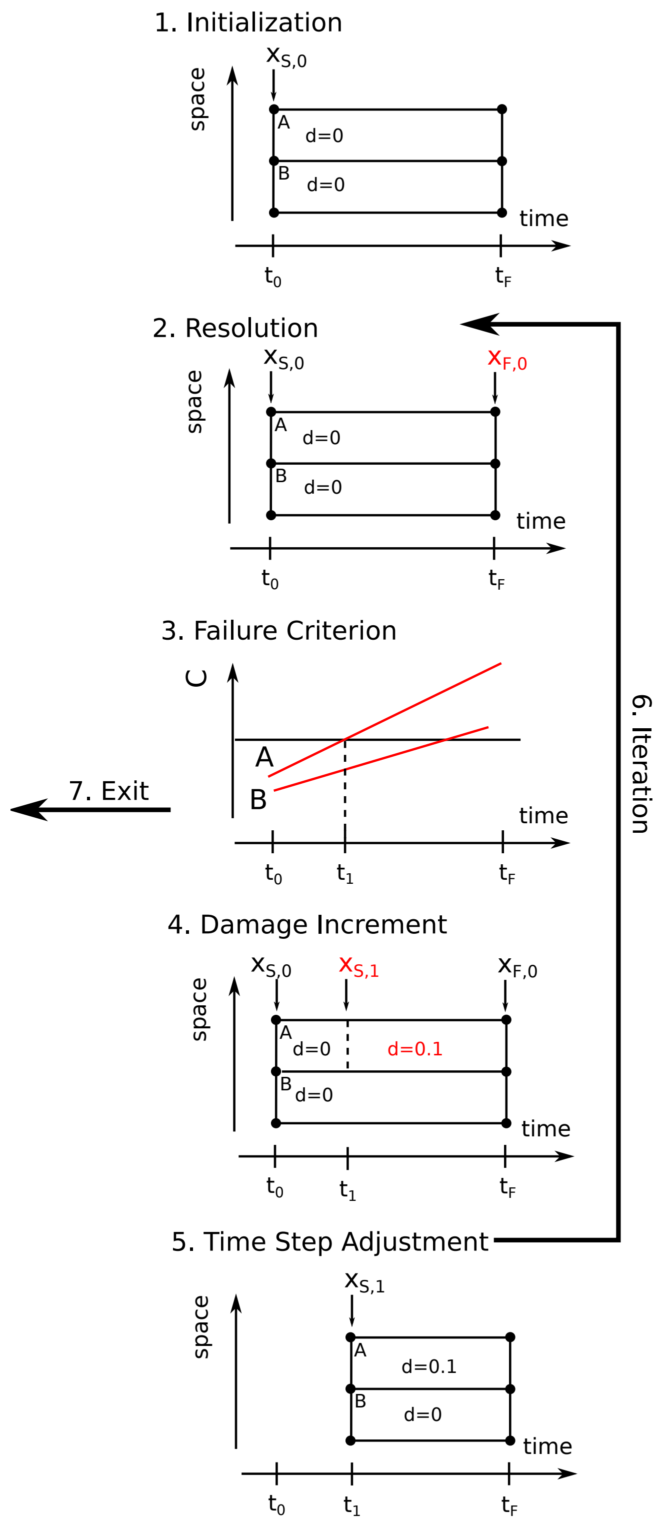

Figure 1: Flowchart of the algorithm with two space-time finite elements (with 1 space dimension). Red indicates values that have been calculated at the corresponding step of the algorithm. Arrows show at which instant corresponds each displacements $\mathbf{x}$.

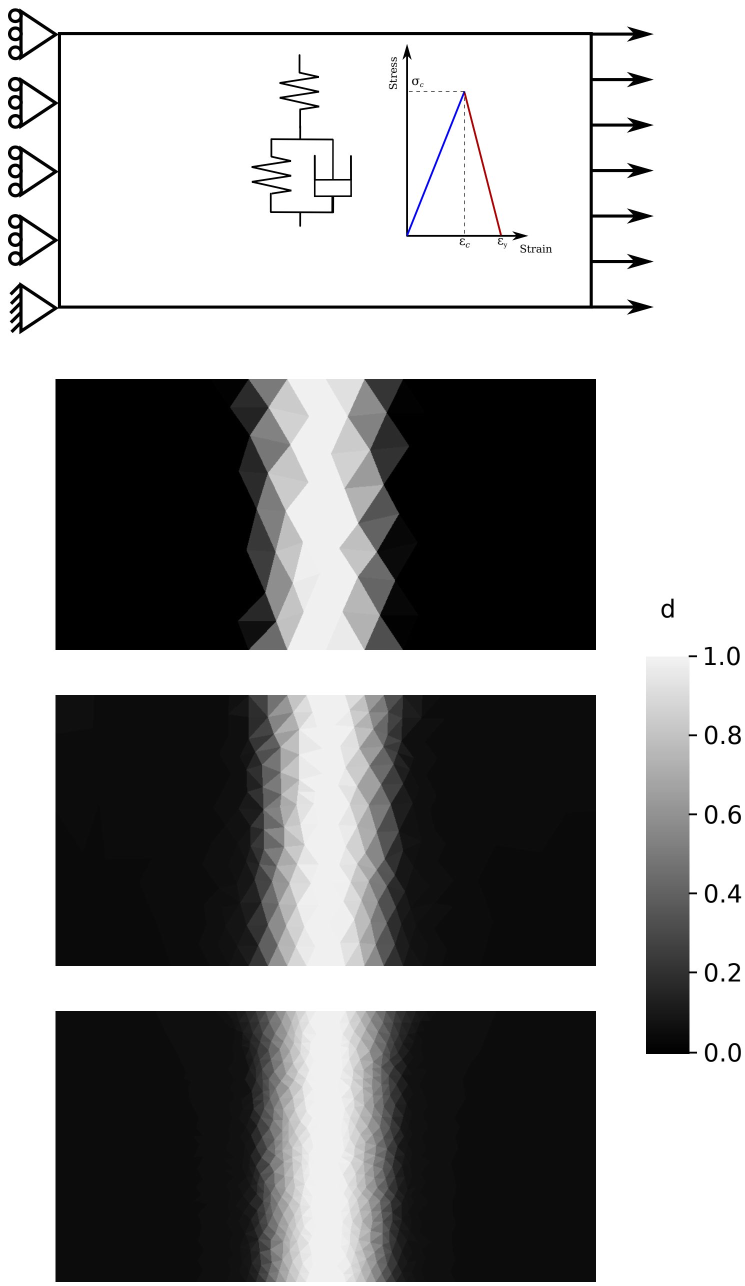

Figure 2: Damage pattern after failure obtained for a uniform plate subject to uni-axial tension with three different mesh sizes. Grey level indicates the value of the scalar damage variable (white = 1). The strength of one element in the center of the plate was reduced by 0.1 % to enforce the location of the damage band.

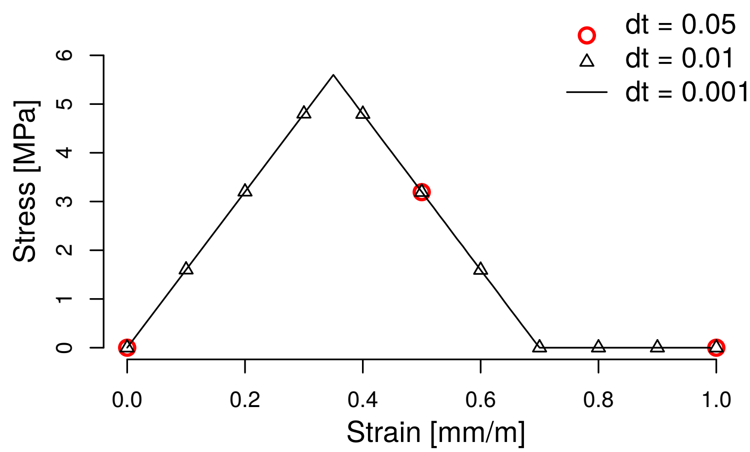

Figure 3: Stress-strain curves for a single element loaded in displacement (constant strain rate) with different time steps. The post-peak behavior is recovered by the algorithm even when the element is loaded beyond its peak.

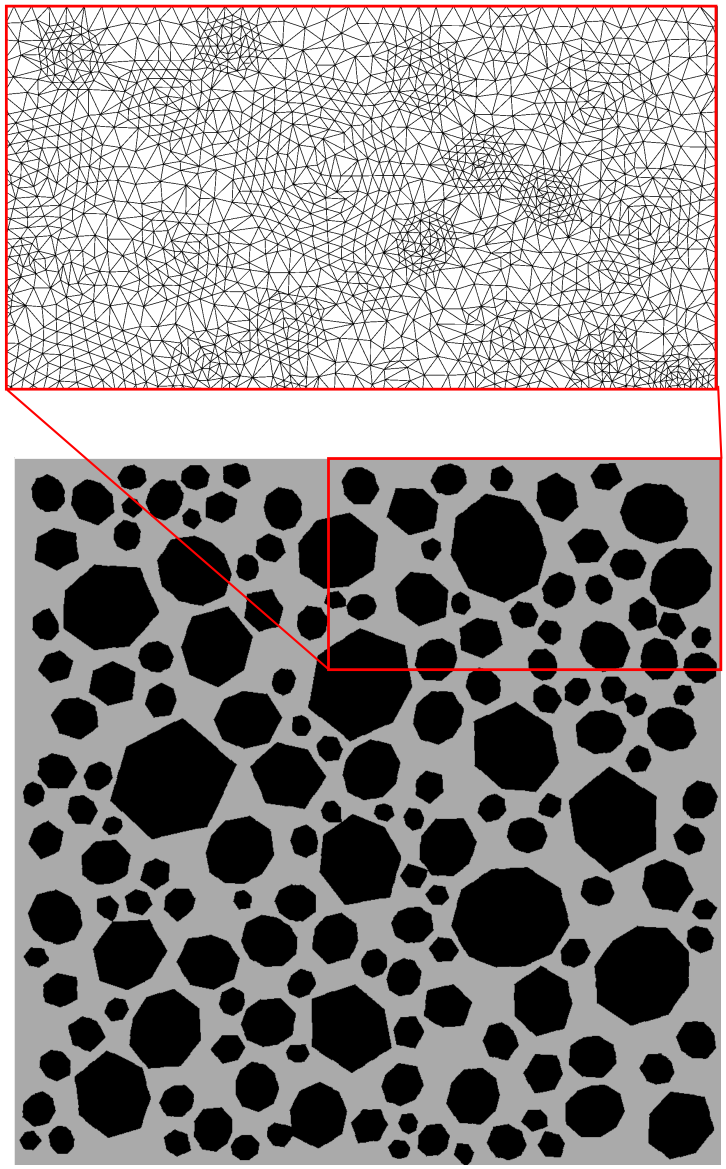

Figure 4: Microstructure and zoom-in on the details of the finite element mesh.

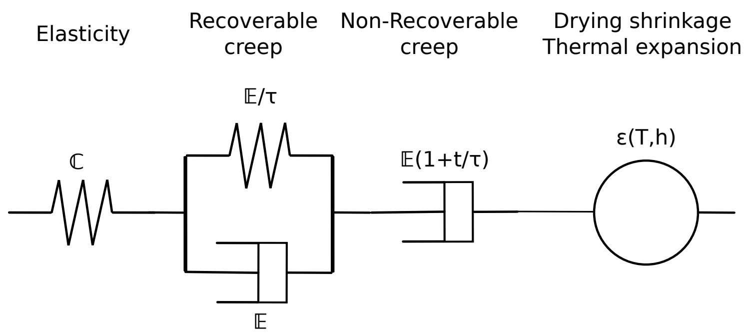

Figure 5: Spring-dashpot model for the cement paste.

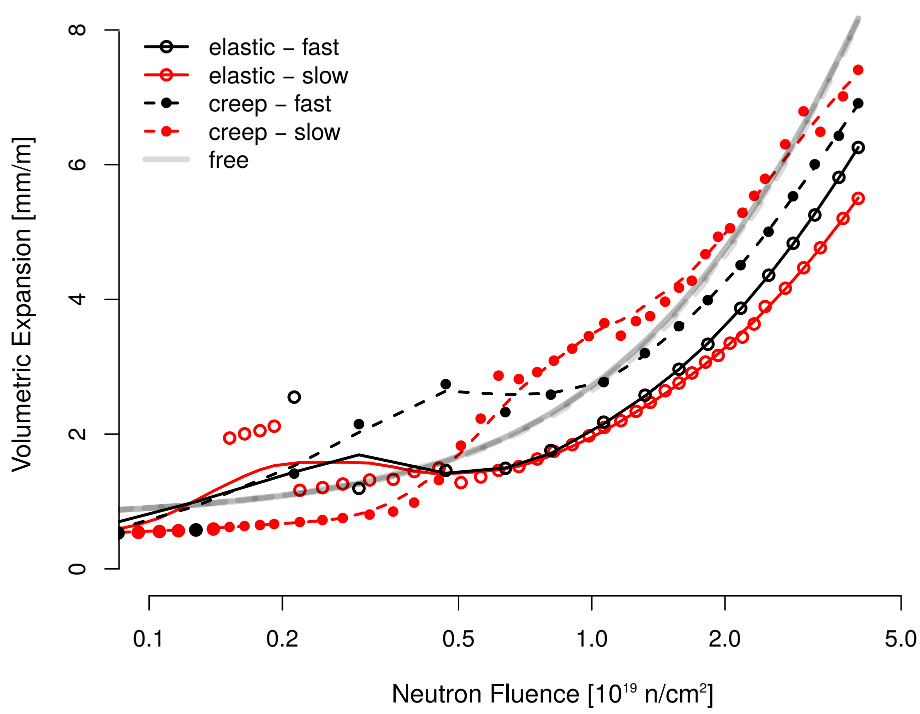

Figure 6: Volumetric expansion as a function of the neutron fluence for the restrained case.

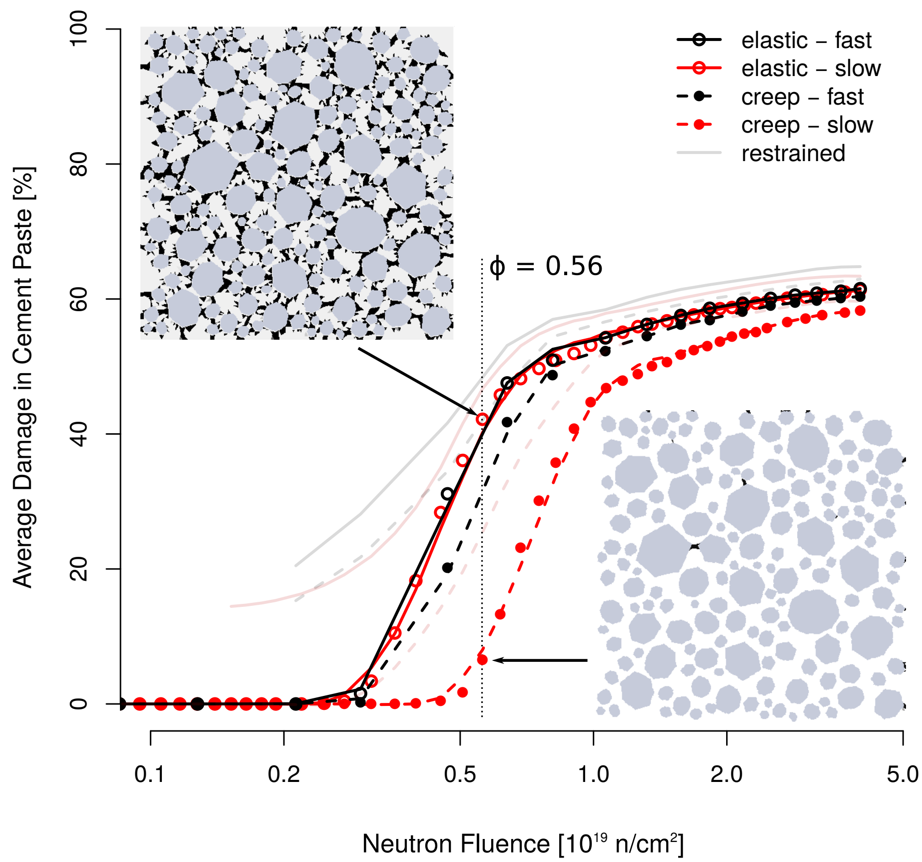

Figure 7: Damage in the cement paste as a function of the fluence for the free boundary condition. Trends for the restrained case are indicated in grey. The microstructures correspond to the free, long-term, elastic simulation (left) and free, long-term, visco-elastic simulation (right) for a neutron fluence of 0.56.

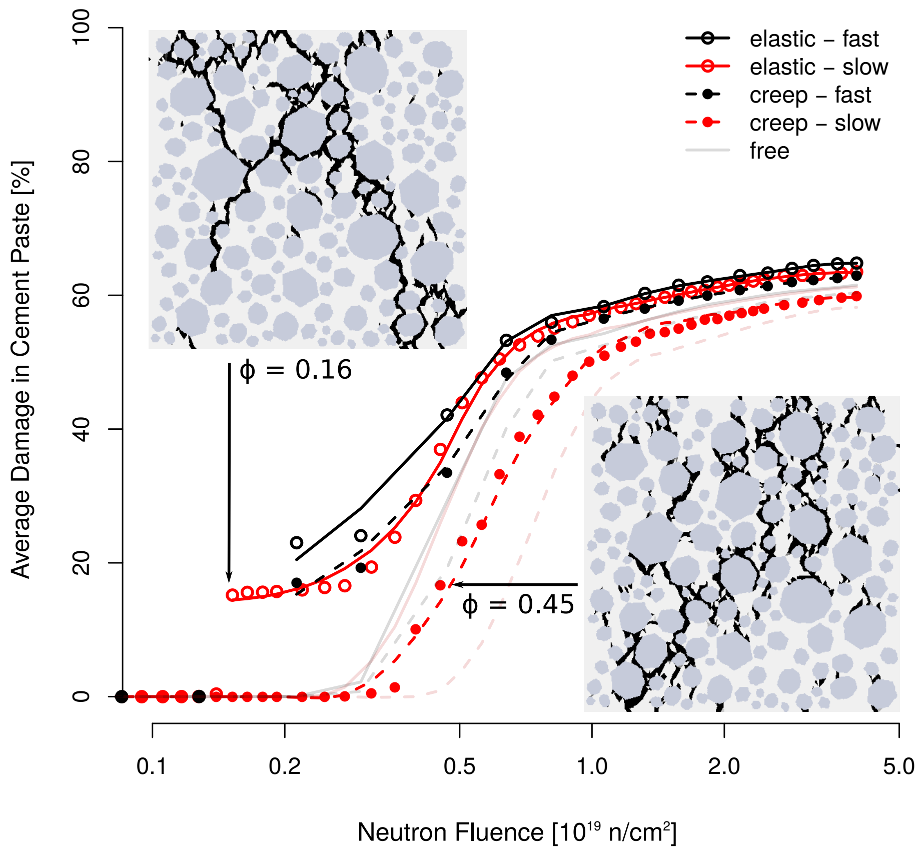

Figure 8: Damage in the cement paste as a function of the fluence for the restrained boundary condition. Trends for the free case are indicated in grey. The microstructures correspond to the restrained, long-term, elastic simulation (left) and restrained, long-term, visco-elastic simulation (right) for the fluence at which the macro-crack percolates.

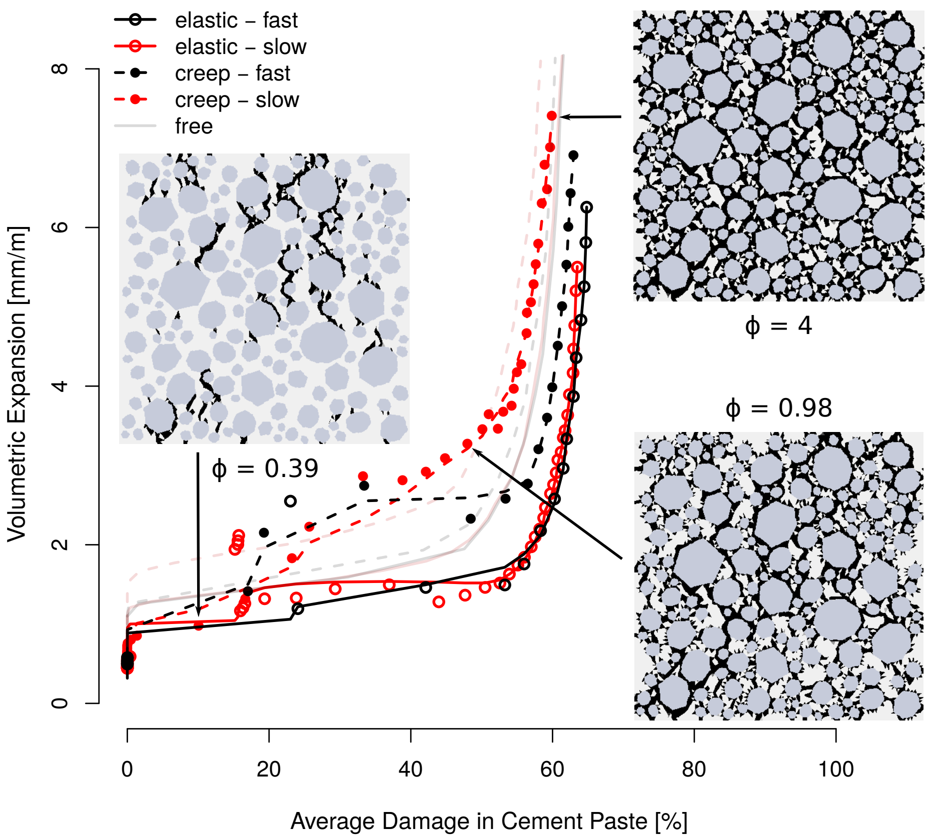

Figure 9: Volumetric expansion as a function of the damage for the restrained case. The microstructures correspond to the restrained, long-term, visco-elastic simulation at three stages of the damage process: initiation and propagation of a compressive macro-crack ($\phi = 0.39$), initiation of diffuse micro-cracks ($\phi = 0.98$) and further opening of the micro-cracks ($\phi = 4$).

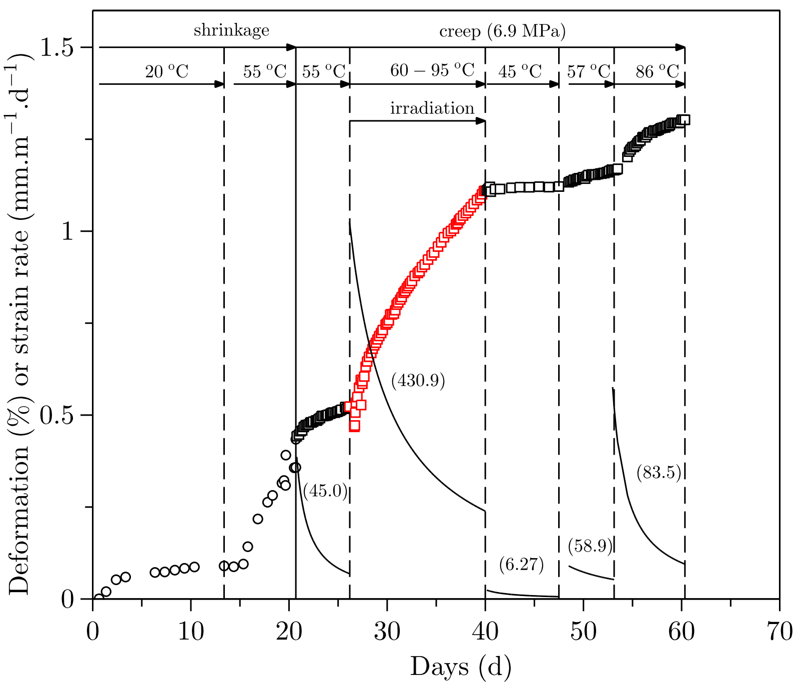

Figure 10: Measured shrinkage (○) and creep (□) strain of Portland cement grout. (□) correspond to creep under irradiation. Reconstructed from Gray's data. Numbers in brackets indicate the creep kinetics parameter, a, given in $\mu\mathrm{m\,m^{-1}\,d^{-1}}$, assuming a logarithmic fit $\varepsilon = \varepsilon_0 + a \log(1 + t - t_0)$. Solids line: creep kinetics.